

OPEN

Solvothermal synthesis of n-type $\text{Bi}_2(\text{Se}_x\text{Te}_{1-x})_3$ nanoplates for high-performance thermoelectric thin films on flexible substrates

Yuki Kimura¹, Ryotaro Mori¹, Susumu Yonezawa¹, Hayato Yabuki¹, Hiromasa Namiki², Yuichi Ota² & Masayuki Takashiri^{1*}

To improve thermoelectric performance of materials, the utilization of low-dimensional materials with a multi-alloy system is a promising approach. We report on the enhanced thermoelectric properties of n-type $\text{Bi}_2(\text{Se}_x\text{Te}_{1-x})_3$ nanoplates using solvothermal synthesis by tuning the composition of selenium (Se). Variation of the Se composition within nanoplates is demonstrated using X-ray diffraction and electron probe microanalysis. The calculated lattice parameters closely followed Vegard's law. However, when the Se composition was extremely high, an impurity phase was observed. At a reduced Se composition, regular-hexagonal-shaped nanoplates with a size of approximately 500 nm were produced. When the Se composition was increased, the shape distribution became random with sizes more than 5 μm . To measure the thermoelectric properties, nanoplate thin films (NPTs) were formed on a flexible substrate using drop-casting, followed by thermal annealing. The resulting NPTs sufficiently adhered to the substrate during the bending condition. The electrical conductivity of the NPTs increased with an increase in the Se composition, but it rapidly decreased at an extremely high Se composition because of the presence of the impurity phase. As a result, the $\text{Bi}_2(\text{Se}_x\text{Te}_{1-x})_3$ NPTs exhibited the highest power factor of $4.1 \mu\text{W}/(\text{cm}\cdot\text{K}^2)$ at a Se composition of $x = 0.75$. Therefore, it was demonstrated that the thermoelectric performance of $\text{Bi}_2(\text{Se}_x\text{Te}_{1-x})_3$ nanoplates can be improved by tuning the Se composition.

With the development of information technology including the Internet of things (IoT), the importance of thermoelectric materials that form flexible thin films has increased. This is because thermoelectric materials can directly convert thermal energy to electrical energy and vice versa. The electrical energy generated from the thermal energy via the Seebeck effect can be used to power wireless and wearable sensors^{1–4}. The thermal energy produced from electrical energy via the Peltier effect can be used to cool electronic devices^{5–7}. In both cases, the energy conversion efficiency depends on the dimensionless figure-of-merit ZT , defined as $ZT = S^2\sigma T/\kappa$, where S is the Seebeck coefficient, σ is the electrical conductivity, κ is the thermal conductivity, and T is the absolute temperature. In addition, the power factor PF defined by $PF = S^2\sigma$ is an important material property.

Among thermoelectric materials, bismuth telluride-based alloys which were developed in the 1950s are the most suitable materials for application to IoT technology^{8–10}. This is because they exhibit the highest thermoelectric properties near 300 K. At this temperature, thermoelectric materials can be used as both thermoelectric generators and Peltier coolers. In particular, ternary alloys such as $\text{Bi}_2(\text{Se}_x\text{Te}_{1-x})_3$ are known to exhibit superior performance compared to binary alloys such as Bi_2Te_3 and Bi_2Se_3 ^{11–14}. Bismuth telluride-based alloys including binary and ternary alloys commonly have rhombohedral tetradymite-type crystal structures with the space group $D_{3d}^5(R\bar{3}m)$ and hexagonal unit cells¹⁵. The crystal structures of Bi_2Te_3 and Bi_2Se_3 binary and $\text{Bi}_2(\text{Se}_x\text{Te}_{1-x})_3$ ternary alloys are presented in the supplemental information provided in Fig. S1. In the Bi_2Te_3 structure, the unit cell is composed of five covalently bonded monatomic sheets along the c -axis in the sequence $-\text{Te}^{(1)}-\text{Bi}-\text{Te}^{(2)}-\text{Bi}-\text{Te}^{(1)}-$. The superscripts (1) and (2) denote the two different chemical states of the anions. The bonds between $\text{Te}^{(1)}$ and

¹Department of Materials Science, Tokai University, 4-1-1 Kitakaname, Hiratsuka, Kanagawa, 259-1292, Japan.

²Tokyo Metropolitan Industrial Technology Research Institute, 2-4-10, Aomi, Koto-ku, Tokyo, 135-0064, Japan.

*email: takashiri@tokai-u.jp

Bi include both covalent and ionic bonds, while Te⁽²⁾ and Bi are covalently bonded. Moreover, a very weak van der Waals attraction exists between neighboring Te⁽¹⁾ layers. In the Bi₂Se₃ structure, only Te atoms are replaced by Se atoms, and the structure of the unit cell is the same as that of the Bi₂Te₃. In the ternary alloys, Bi₂(Se_xTe_{1-x})₃ is formed via the preferential replacement of Se atoms with Te⁽²⁾ atoms. When the Se atoms fully occupied the Te⁽²⁾ sites, they begin to fill the Te⁽¹⁾ sites.

To further enhance the thermoelectric properties, an effective approach is to reduce the dimension of the materials. Hicks *et al.* theoretically predicated that materials with low dimensions exhibit improved thermoelectric properties due to the increased power factor caused by quantum confinement¹⁶. However, the difficulty of device fabrication and the fabrication cost increase as the dimension is significantly reduced. Considering these factors, 2D materials including layered structure and nanoplates have recently attracted broad attention^{17–20}. In particular, nanoplates are highly suitable because they can be used to fabricate high-quality single crystals via a low-cost wet process^{21–26}. As such, nanoplates made of bismuth telluride-based ternary alloys are promising thermoelectric materials. Soni *et al.* and Liu *et al.* prepared Bi₂Te_{3-x}Se_x nanoplates by varying the atomic composition using a polyol process^{27,28}. Hong *et al.* prepared similar nanoplates using a microwave-assisted solvothermal method²⁹. The bulk sintered samples were fabricated from Bi₂(Se_xTe_{1-x})₃ nanoplates and exhibited excellent thermoelectric performances. These pioneering studies partially motivated our own investigation into Bi₂Te_{3-x}Se_x nanoplates with optimal atomic composition to form flexible thin films for application toward IoT technology. In addition, these studies motivated us to investigate the thermoelectric properties of nanoplates while maintaining their shape. In our previous reports, we fabricated binary alloy nanoplates such as Bi₂Te₃ and Sb₂Te₃ using solvothermal synthesis and estimated their thermoelectric properties^{30–32}.

In this study, we fabricated n-type Bi₂(Se_xTe_{1-x})₃ nanoplates using solvothermal synthesis while significantly changing the atomic composition. The resulting nanoplates were used to form thin films on a flexible substrate using drop-casting. The structural and thermoelectric properties of Bi₂(Se_xTe_{1-x})₃ nanoplate thin films (NPTs) were evaluated and the optimal atomic composition was determined.

Methods

Bi₂(Se_xTe_{1-x})₃ nanoplates were synthesized via a solvothermal process³³. The outline of this process is described in the supplemental information provided in Fig. S2. We used Bi₂O₃ (Fujifilm Wako Pure Chemical Co., >99.9%), TeO₂ (Kojundo Chemical Laboratory Co., Ltd., >99.9%), SeO₂ (Fujifilm Wako Pure Chemical Co., >97.0%), ethylene glycol (Fujifilm Wako Pure Chemical Co., >90.0%), polyvinyl pyrrolidone (PVP) (Fujifilm Wako Pure Chemical Co., K30, M_n ~40,000), and sodium hydroxide (NaOH) (Fujifilm Wako Pure Chemical Co., >97.0%) to prepare the precursor liquid-solution. The typical procedure for the synthesis of Bi₂(Se_xTe_{1-x})₃ nanoplates is as follows: 0.4 g PVP was dissolved in ethylene glycol (18 mL), followed by the addition of Bi₂O₃ (20 mM), TeO₂ (5.4–55.2 mM), SeO₂ (5.4–55.2 mM), and 2 mL of NaOH liquid-solution (0.5 M). Eleven samples of Bi₂(Se_xTe_{1-x})₃ nanoplates were prepared while the atomic composition of Se was changed from $x = 0.08$ to 0.92. It is to be noted that the pure Bi₂Te₃ nanoplates ($x = 0$) and their thin films were prepared in our previous reports, and the structural and thermoelectric properties were discussed³⁴. However, it was possible to fabricate the pure Bi₂Se₃ nanoplates ($x = 1.0$) using the solvothermal method in our process. The resulting precursor liquid-solutions were sealed in an autoclave, heated, and maintained at 200 °C for 20 h with stirring of the liquid-solution at 500 rpm. After the solvothermal synthesis, the liquid-solutions were naturally cooled to below 50 °C. The nanoplates were then collected via centrifugation and washed several times in distilled water and absolute ethanol. Finally, they were dried in vacuum at 60 °C for 1 day.

The phase purity and crystal structure of Bi₂(Se_xTe_{1-x})₃ nanoplates were characterized by X-ray diffraction (XRD, Bruker D8 ADVANCE) using Cu-K_α radiation ($\lambda = 0.154$ nm) at a scanning rate of 0.03°/s with 2θ ranging from 10° to 80°. The atomic composition of the nanoplates was examined using an electron probe micro analyzer (EPMA, Shimadzu EPMA-1610). The compositions of the samples were calibrated using the installed ZAF4 program of the EPMA-1610. The surface morphology of the Bi₂(Se_xTe_{1-x})₃ nanoplates was investigated using a field emission scanning electron microscopy (FESEM, Hitachi S-4800).

To measure the thermoelectric properties of the Bi₂(Se_xTe_{1-x})₃ nanoplates, NPTs were prepared via drop-casting^{35,36}. The outline of the drop-casting process is described in the supplemental information provided in Fig. S3. Then, 30 mg of nanoplates were ultrasonically dispersed in 3.0 mL of methanol to form the Bi₂(Se_xTe_{1-x})₃ nanoplate ink. The nanoplate ink was deposited on a polyimide substrate using a plastic enclosure so that the NPTs were thick with a uniform thickness. The average thickness of NPTs is approximately 4 μm and the standard deviation is 0.3 μm. After drying the NPTs in air, thermal annealing was performed to evaporate the residual matter in the NPTs and to connect the nanoplates to each other, based on our previous study³⁷. A furnace was filled with a mixture of argon (95%) and hydrogen (5%) at atmospheric pressure. The gas flow rate was maintained at 1.0 slm throughout the annealing process. The temperature was maintained at 250 °C, and a heating rate of 4 K/min was used; the samples were annealed at the set temperature for 1 h. After thermal annealing, the samples were naturally cooled to below 70 °C. In our previous report, we confirmed that the atomic composition of the nanoplates did not change during thermal annealing at 250 °C³⁷.

The in-plane Seebeck coefficient S of the Bi₂(Se_xTe_{1-x})₃ NPTs was measured near 300 K with accuracy of ±5%. One end of the thin film was connected to a heat sink and the other end to a heater. The Seebeck coefficient was determined as the ratio of the potential difference (ΔV) along the film to the temperature difference (ΔT). The in-plane electrical conductivity σ of the NPTs was measured near 300 K using a four-point probe method (Napson, RT-70V) with accuracy of ±3%. The in-plane power factor σS^2 was obtained from the experimentally measured Seebeck coefficient and electrical conductivity. The carrier concentration n and mobility μ were measured using the van der Pauw's method (HM-055, Ecopia).

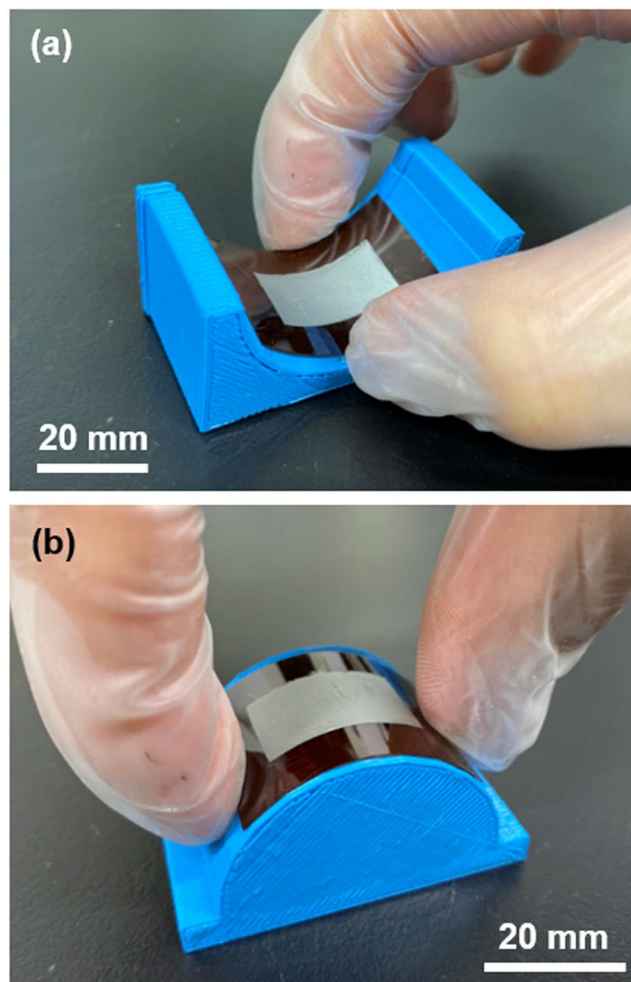


Figure 1. Images of typical $\text{Bi}_2(\text{Se}_x\text{Te}_{1-x})_3$ nanoplate thin film ($x = 0.75$) on polyimide substrate for a bending condition. **(a)** Concave shape with a curvature radius of 20 mm, **(b)** convex shape with a curvature radius of 20 mm.

Results and discussion

An image of a typical $\text{Bi}_2(\text{Se}_x\text{Te}_{1-x})_3$ nanoplate thin film ($x = 0.75$) on a polyimide substrate is shown in Fig. 1. The thin film firmly adhered to the substrate applying compressive stress (Fig. 1(a)) and tensile stress (Fig. 1(b)). To use NPTs in real-world applications, we conducted bending tests by applying compressive stress and tensile stress on the NPTs possessing a high power factor. When the NPTs were repeatedly bent 450 times, the relative variation of resistance was measured. The detailed experimental setup and results are shown in Fig. S4. As a result, the relative resistance after the bending (450 times) was approximately two times higher than that of the initial resistance along both stressing directions. No peeling behavior was observed in the NPTs after the completion of the bending tests.

X-ray diffraction (XRD) patterns of the $\text{Bi}_2(\text{Se}_x\text{Te}_{1-x})_3$ nanoplates with different Se compositions are shown in Fig. 2(a). The diffraction peaks of the $\text{Bi}_2(\text{Se}_x\text{Te}_{1-x})_3$ nanoplates ($x = 0.08$) can be closely indexed as the rhombohedral Bi_2Te_3 phase (JCPDS No. 15-0863), and no other phases were observed. As the Se composition increased until $x = 0.75$, the detected peaks gradually shifted to the higher angle, and other phases were not observed. This indicates that the Te atoms were replaced by the Se atoms in the unit cell, and the unit cell volume decreased because the atomic radius of Se is smaller than that of Te. Therefore, we conclude that the ternary alloy system of $\text{Bi}_2(\text{Se}_x\text{Te}_{1-x})_3$ was successfully synthesized in this composition region. When the Se composition exceeded $x = 0.83$, another phase of $\text{Bi}_2\text{Se}_2\text{Te}$ (JCPDS No. 57-0622) with a skippenite crystal structure was observed owing to the disordered occupation of Te/Se atoms in the quintuple layer³⁸. The $\text{Bi}_2\text{Se}_2\text{Te}$ crystals are usually used as topological insulators^{39,40}. To perform a detailed analysis of the crystal structure, the enlarged views of the 006 and 015 peaks are presented in Fig. 2(b,c), respectively. The vertical dashed lines and dashed-dotted lines in the figures represent the peak positions of Bi_2Te_3 (JCPDS No. 15-0863) and Bi_2Se_3 (JCPDS No. 33-0214), respectively. It is clearly seen that both peaks are shifted from the dashed lines to the dashed-dotted lines with the increase in the Se composition. This indicates that the lattice parameters decreased with increasing Se composition.

Based on the results in Fig. 2(b,c), we calculated the lattice parameters a and c . Figure 3 shows the relationship between the Se composition in $\text{Bi}_2(\text{Se}_x\text{Te}_{1-x})_3$ and the lattice parameters. The dashed lines correspond to Vegard's

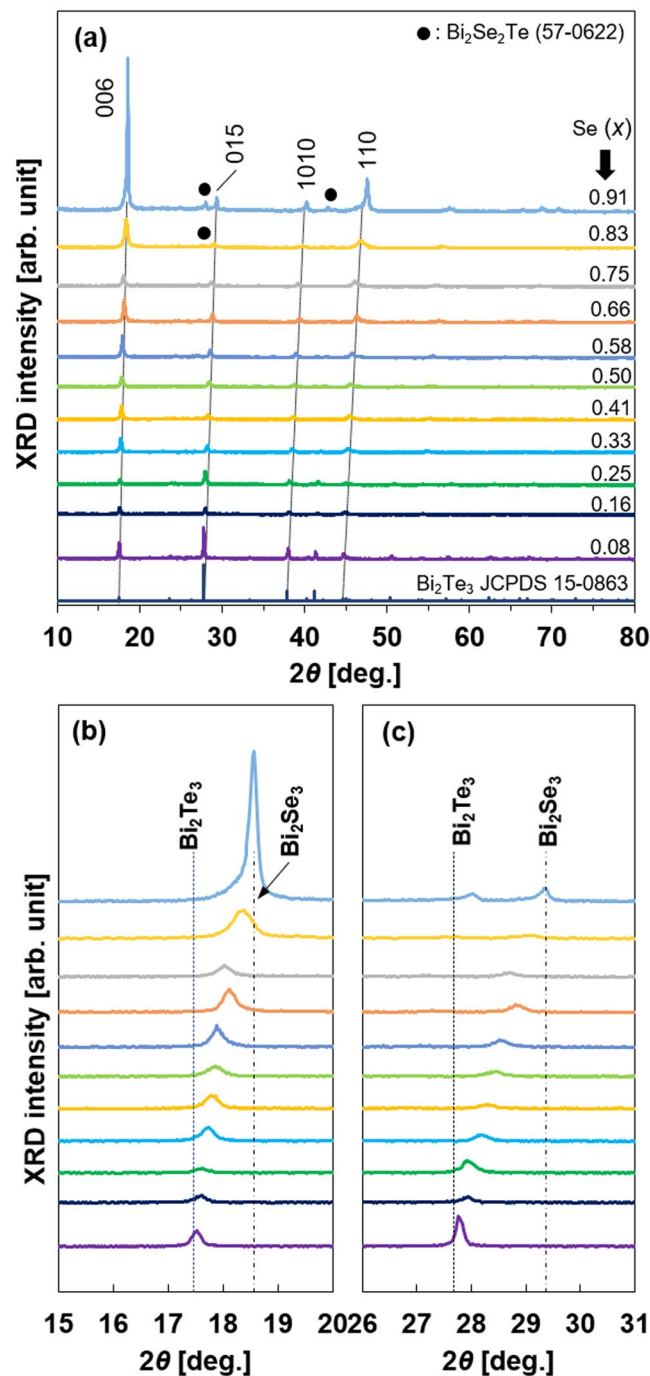


Figure 2. XRD patterns of the $\text{Bi}_2(\text{Se}_x\text{Te}_{1-x})_3$ nanoplates obtained at various Se compositions. (a) 2θ : $10\text{--}80^\circ$, (b) 2θ : $15\text{--}20^\circ$, (c) 2θ : $26\text{--}31^\circ$.

law. In Fig. 3(a), the lattice parameter a is consistent with Vegard's law over the entire range of Se compositions. However, in Fig. 3(b), the lattice parameter c exhibits a positive deviation over the range from Se composition $x = 0.42$ to 0.83 . A similar phenomenon was reported in bulk samples by Wiese *et al.*⁴¹. This observation was explained in terms of Se-atom substitution in preferred planes in the range $\text{Bi}_2\text{Te}_3\text{--Bi}_2\text{Te}_2\text{Se}$. Therefore, the trend shown in Fig. 3(b) occurred not only in the nanoplates (2D material) but also in the bulk samples (3D material).

The relationship between the Se composition in the liquid-solution for solvothermal synthesis and the corresponding nanoplates is shown in Fig. 4(a). The diagonal dashed line in this figure represents identical Se composition in both the liquid-solution and the nanoplate. The Se composition in the nanoplates increased as their composition in the liquid-solution was increased along the diagonal line. Therefore, the successful synthesis of a ternary alloy system of $\text{Bi}_2(\text{Se}_x\text{Te}_{1-x})_3$ was proved using the EPMA. It should be noted that most of the plots exceeded the diagonal dashed line. This indicates that Se atoms are more easily incorporated into the nanoplate crystals than the Te atoms because the former has a smaller radius and higher electronegativity compared to

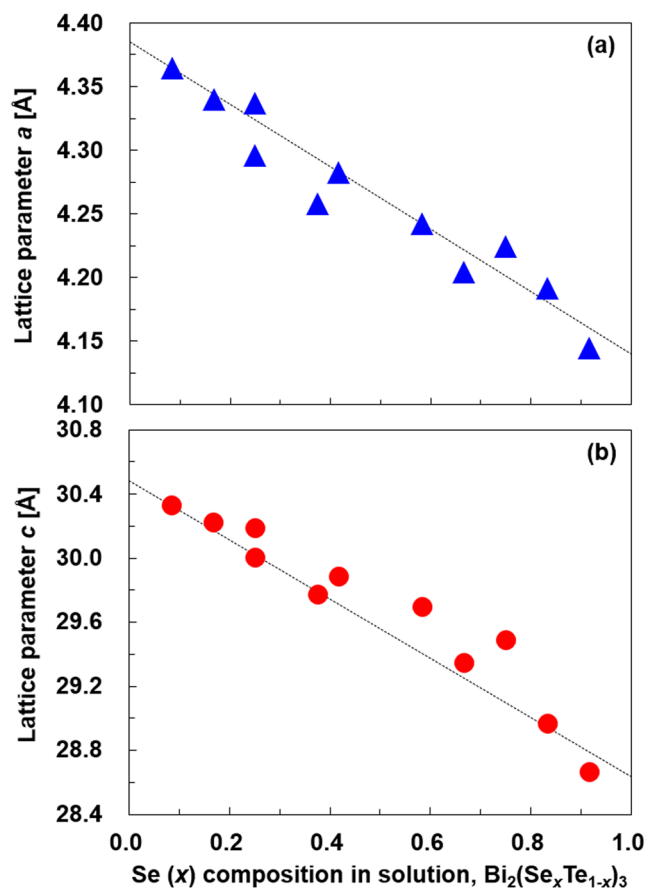


Figure 3. Lattice parameters of $\text{Bi}_2(\text{Se}_x\text{Te}_{1-x})_3$ nanoplates for various Se compositions, measured from the XRD peaks. (a) *a*-axis and (b) *c*-axis.

the latter²⁶. In Fig. 4(b), the relationship between the Se composition in the liquid-solution and the (Se + Te)/(Bi + Se + Te) ratio in the corresponding nanoplates is presented. The horizontal dashed line represents the stoichiometric proportion of $\text{Bi}_2(\text{Se}_x\text{Te}_{1-x})_3$. The (Se + Te)/(Bi + Se + Te) ratio in the nanoplates exhibited a slightly positive deviation from the stoichiometric proportion when the Se composition in liquid-solution was over $x = 0.42$. At a Se composition of $x = 0.92$, the ratio increased, possibly because another phase of $\text{Bi}_2\text{Se}_2\text{Te}$ appeared.

Figure 5 shows surface SEM images of typical $\text{Bi}_2(\text{Se}_x\text{Te}_{1-x})_3$ nanoplates. At a Se composition of $x = 0.08$, high-quality regular-hexagonal nanoplates with diameter of approximately 500 nm and thicknesses less than 50 nm are observed in Fig. 5(a). An enlarged image of the nanoplates is shown in the inset of Fig. 5(a). A screw-dislocation-driven spiral growth appears on the nanoplate's surface. A similar phenomenon was reported in previous studies of Bi_2Se_3 and Sb_2Te_3 nanoplates^{42,43}. In addition, the radius of critical nucleus r_c can be calculated from the spacing between two neighboring turns λ , giving $\lambda = 19r_c$ ⁴⁴. In this case, the measured λ was 23 nm, so that r_c is determined to be approximately 1.2 nm, which is 2.8 times larger than the lattice parameter *a* in a unit cell with a corresponding Se composition. When the Se composition was increased from $x = 0.25$ to 0.58, the edge size of the nanoplates increased and their shape gradually deviated from regular hexagon (Fig. 5(b–d)). When the Se composition was further increased to $x = 0.75$, the variation of the plate size increased from 0.5 to 3 μm , and the shape of the plates became random (Fig. 5(e)). In addition, when the Se composition had the highest value ($x = 0.92$), the nanoplates gathered to form large plates with a size more than 5 μm (Fig. 5(f)). Thus, although the detailed mechanism of the crystal growth was not elucidated, the experimental results clearly show differences in the shape and size of the nanoplates depending on the Se composition. A possible growth mechanism of the $\text{Bi}_2(\text{Se}_x\text{Te}_{1-x})_3$ nanoplates is as follows: when the Se composition is relatively low, the Se atoms smoothly replaced the Te atoms at the $\text{Te}^{(2)}$ sites. During this process, the regular hexagonal shape of the nanoplates was sustained. After the Se atoms fully occupied the $\text{Te}^{(2)}$ sites, these atoms generally began to fill the $\text{Te}^{(1)}$ sites via disordered occupation of Te/Se atoms. As a result, the crystal growth of nanoplates is disordered, and consequently, the shape and size of the nanoplates became random. On further increasing the Se composition, the $\text{Bi}_2\text{Se}_2\text{Te}$ phase was also present and the shape was completely different from hexagonal⁴⁵.

Figure 6 shows the relationship between the Se atomic composition and the in-plane thermoelectric properties of the $\text{Bi}_2(\text{Se}_x\text{Te}_{1-x})_3$ NPTs on a polyimide substrate. The Seebeck coefficient of the $\text{Bi}_2(\text{Se}_x\text{Te}_{1-x})_3$ NPTs as a function of Se composition is shown in Fig. 6(a). For all Se compositions, the samples exhibited negative values. This is indicative of the n-type semiconducting characteristics of the samples. The highest Seebeck coefficient of $-128.6 \mu\text{V/K}$ was obtained for a Se composition of $x = 0.58$. In contrast, the lowest absolute values of $-82.0 \mu\text{V/K}$

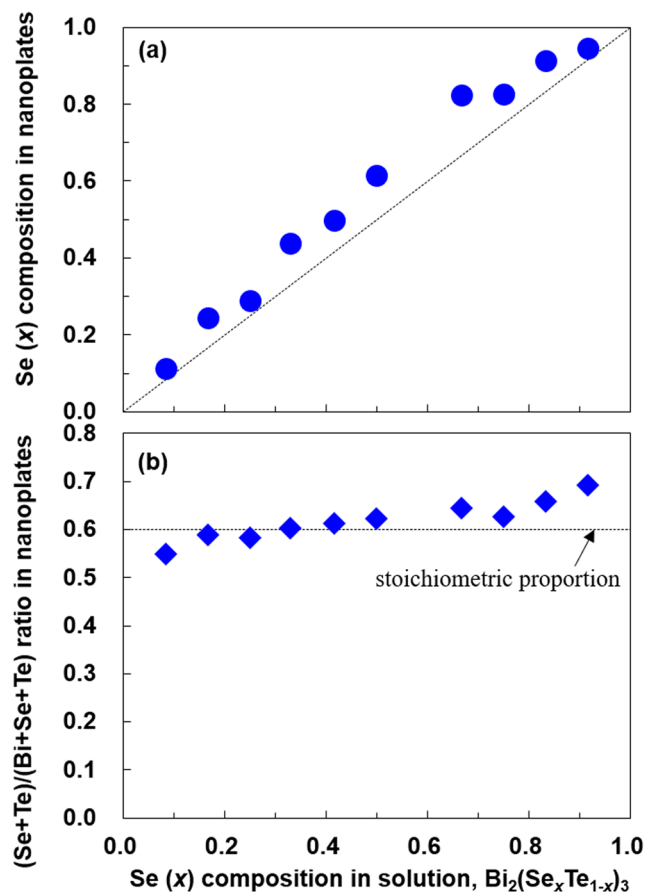


Figure 4. (a) Se composition in nanoplates and (b) (Se + Te)/(Bi + Se + Te) ratio of $\text{Bi}_2(\text{Se}_x\text{Te}_{1-x})_3$ nanoplates as a function of the Se composition in solution, measured using EPMA.

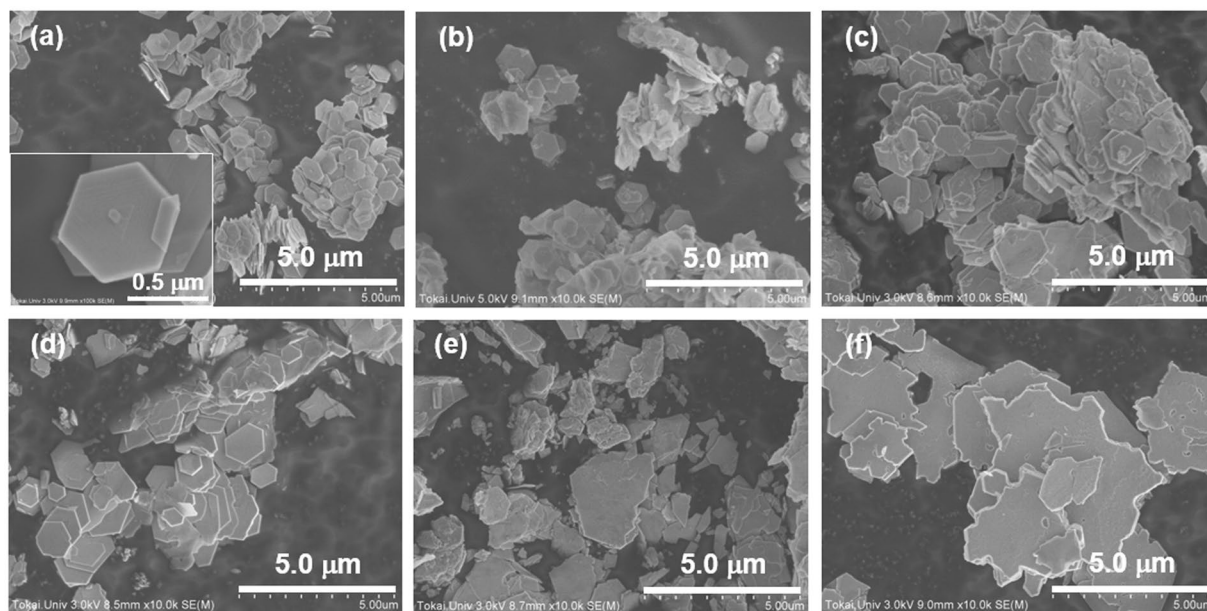


Figure 5. Surface SEM images of the $\text{Bi}_2(\text{Se}_x\text{Te}_{1-x})_3$ nanoplates. (a), (b), (c), (d), (e), and (f) corresponding to the Se composition of $x = 0.08, 0.25, 0.41, 0.58, 0.75, 0.92$, respectively.

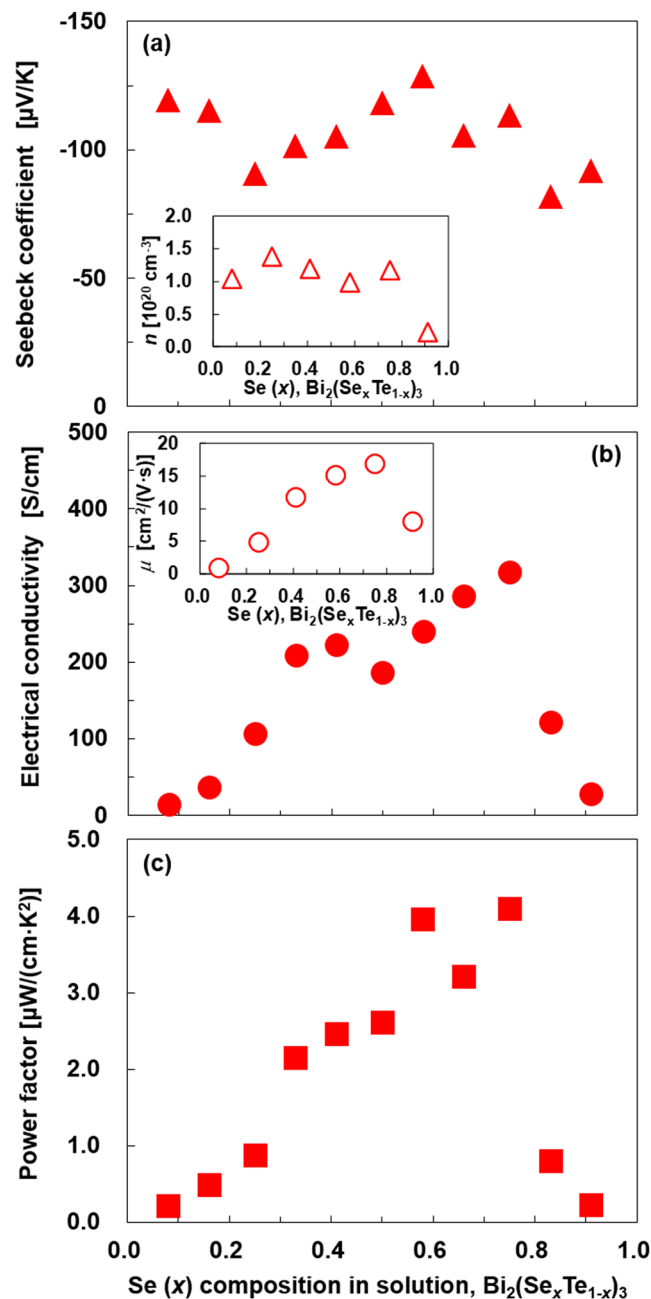


Figure 6. Experimentally measured and calculated thermoelectric properties of the $\text{Bi}_2(\text{Se}_x\text{Te}_{1-x})_3$ thin films as a function of Se composition. (a) Seebeck coefficients, (b) electrical conductivities, and (c) power factors. The carrier concentration and mobility as a function of Se composition are shown in the insets of Fig. 6 (a) and (b), respectively.

was obtained for a Se composition of $x=0.83$. Thus, a clear relationship between the Se composition and the Seebeck coefficient was not observed. This is because the Seebeck coefficient is strongly related to the carrier concentration, as shown in the inset of Fig. 6(a), which fluctuates with the atomic composition. In addition, defects such as Bi and Te vacancies and antisite defects may also affect the carrier concentration. Especially, the antisite defects are relatively easy to form compared to the vacancies because the formation energy of antisite defects is lower than that of vacancies based on the first-principles studies^{46,47}. The NPTs for Se compositions of $x=0.83$ and 0.92 exhibited lower Seebeck coefficients because of the presence of the $\text{Bi}_2\text{Se}_2\text{Te}$ phase⁴⁸.

As shown in Fig. 6(b), the electrical conductivity of the nanoplate thin film at the lowest Se composition ($x=0.08$) was 15 S/cm. When the Se composition was increased to $x=0.75$, the electrical conductivity also increased. The highest electrical conductivity of the thin film was 317 S/cm at a Se composition of 0.75. In general, the electrical conductivity of the alloy system tends to decrease as the number of elements and the atomic composition increase because electron scattering is enhanced²⁸. However, the experimental results show that the electrical conductivity tends to be higher as the Se composition is increased. This is because the mobility, as shown

in the inset of Fig. 6(b), increased due to the increase in the size of the plates. When the Se composition is further increased in excess of $x=0.83$, the electrical conductivity drastically decreases even though the size of the plates increases. One possible explanation is that the $\text{Bi}_2\text{Se}_2\text{Te}$ phase, which is known to achieve large bulk resistivity as a topological insulator^{49,50}, disturbed the electron transport.

Figure 6(c) shows the power factor of the $\text{Bi}_2(\text{Se}_x\text{Te}_{1-x})_3$ NPTs. The relationship between the power factor and Se composition is similar to that between the electrical conductivity and the Se composition. The power factor increased as the Se composition was increased. At a Se composition of $x=0.75$, the power factor exhibited the highest value of $4.1 \mu\text{W}/(\text{cm}\cdot\text{K}^2)$. On further increasing the Se composition, the power factor drastically decreased due to the reduced electrical conductivity.

Conclusions

In summary, n-type $\text{Bi}_2(\text{Se}_x\text{Te}_{1-x})_3$ nanoplates were prepared using solvothermal synthesis while significantly changing the atomic composition. Based on XRD analysis, it was determined that the mixed crystal system of $\text{Bi}_2(\text{Se}_x\text{Te}_{1-x})_3$ was successfully synthesized for all Se compositions and these results were supported by analysis using an EPMA. However, when the Se composition was extremely high, the impurity phase appeared. SEM analysis revealed that the shape of the nanoplates changed from a regular hexagon to an irregular shape as the Se composition was increased. The $\text{Bi}_2(\text{Se}_x\text{Te}_{1-x})_3$ NPTs were formed on a flexible substrate using drop-casting, followed by thermal annealing. They could not be detached from the substrate even after bending. The electrical conductivity of NPTs increased with the increase in the Se composition but rapidly decreased at a high Se composition. As a result, the $\text{Bi}_2(\text{Se}_x\text{Te}_{1-x})_3$ nanoplate thin film exhibited the highest power factor of $4.1 \mu\text{W}/(\text{cm}\cdot\text{K}^2)$ at a Se composition of $x=0.75$. We demonstrated that thermoelectric performance can be improved by optimizing the Se composition. The apertures between the NPTs need to be filled with layers composing bismuth-telluride family of compounds using electrodeposition or other deposition methods to well enhance the thermoelectric performance of the NPTs.

Received: 1 January 2020; Accepted: 30 March 2020;

Published online: 14 April 2020

References

- Roundy, S., Wright, K. P. & Rabaey, A. A study of low level vibrations as a power source for wireless sensor nodes. *J. Comput. Commun.* **11**, 1131–1144 (2003).
- Paradiso, A. J. & Starner, T. Energy scavenging for mobile and wireless electronics. *IEEE Pervasive Comput.* **4**, 18–27 (2005).
- Francioso, L. *et al.* Flexible thermoelectric generator for ambient assisted living wearable biometric sensors. *J. Power Sources.* **196**, 3239–3243 (2011).
- Weber, J. *et al.* Coin-size coiled-up polymer foil thermoelectric power generator for wearable electronics. *Sens. Actuators. A* **132**, 325–330 (2006).
- Riffat, S. B. & Ma, X. Thermoelectrics: a review of present and potential applications. *Appl. Therm. Eng.* **23**, 913–935 (2003).
- Bell, L. E. Cooling, heating, generating power, and recovering waste heat with thermoelectric systems. *Science.* **321**, 1457–1461 (2008).
- Lin, X. *et al.* Experimental study and Taguchi analysis on LED cooling by thermoelectric cooler integrated with microchannel heat sink. *Appl. Energy* **242**, 232–238 (2019).
- Harman, T. C., Paris, B., Miller, S. E. & Goering, H. L. Preparation and some physical properties of Bi_2Te_3 , Sb_2Te_3 , and As_2Te_3 . *J. Phys. Chem. Solids.* **2**, 181–190 (1957).
- Satterthwaite, C. B. & Ure, R. W. Jr Electrical and thermal properties of Bi_2Te_3 . *Phys. Rev.* **108**, 1164–1170 (1957).
- Goldsmid, H. J. & Douglas, R. W. The use of semiconductors in thermoelectric refrigeration. *Br. J. Appl. Phys.* **5**, 386–390 (1954).
- Yim, W. M. & Rosi, F. D. Compound tellurides and their alloys for Peltier cooling - a review. *Solid State Elec.* **15**, 1121–1140 (1972).
- Yashima, I., Watanabe, H., Ogisu, T., Tsukuda, R. & Sato, S. Thermoelectric properties and Hall effect of $\text{Bi}_2\text{Te}_{3-x}\text{Se}_x$ polycrystalline materials prepared by a hot press method. *Jpn. J. Appl. Phys.* **37**, 2472–2473 (1998).
- Takashiri, M. *et al.* Comparison of crystal growth and thermoelectric properties of n-type Bi-Se-Te and p-type Bi-Sb-Te nanocrystalline thin films: Effects of homogeneous irradiation with an electron beam. *J. Appl. Phys.* **115**, 214311 (2014).
- Pan, Y., Wei, T. R., Wu, C. F. & Li, J. F. Electrical and thermal transport properties of spark plasma sintered n-type $\text{Bi}_2\text{Te}_{3-x}\text{Se}_x$ alloys: the combined effect of point defect and Se content. *J. Mater. Chem. C* **3**, 10583–10589 (2015).
- H. Scherrer, S. Scherrer, CRC Handbook of Thermoelectrics, in: D.M. Rowe (Ed.), CRC Press LLC, Boca Raton 211–238 (1995).
- Hicks, L. D. & Dresselhaus, M. S. Effect of quantum-well structure on the thermoelectric figure of merit. *Phys. Rev. B* **47**, 12727 (1993).
- Svechnikova, T. E. *et al.* Crystal growth and thermoelectric properties of tetradymite-like layered chalcogenides and $(\text{Bi}_2\text{Te}_3)_{1-x}(\text{Sb}_2\text{Te}_3)_x(\text{Sb}_2\text{Se}_3)_x$ solid solutions. *Inorg. Mater.* **42**, 1311–1317 (2006).
- Matsuoka, K., Okuhata, M. & Takashiri, M. Dual-bath electrodeposition of n-type Bi-Te/Bi-Se multilayer thin films. *J. Alloys Compd.* **649**, 721–725 (2015).
- Fan, X. A. *et al.* Bi_2Te_3 hexagonal nanoplates and thermoelectric properties of n-type Bi_2Te_3 nanocomposites. *J. Phys. D: Appl. Phys.* **40**, 5975–5979 (2007).
- Takashiri, M., Tanaka, S. & Miyazaki, K. Growth of single-crystalline bismuth antimony telluride nanoplates on the surface of nanoparticle thin films. *J. Cryst. Growth.* **372**, 199–204 (2013).
- Jin, R., Chen, G., Pei, J., Xu, H. & Lv, Z. S. Solvothermal synthesis and growth mechanism of ultrathin Sb_2Te_3 hexagonal nanoplates with thermoelectric transport properties. *RSC Adv.* **2**, 1450–1456 (2012).
- Liu, S. *et al.* Fabrication of Cu-doped Bi_2Te_3 nanoplates and their thermoelectric properties. *J. Electron. Mater.* **46**, 2697–2704 (2017).
- Liu, J. L. *et al.* High performance visible photodetectors based on thin two-dimensional Bi_2Te_3 nanoplates. *J. Alloys Compd.* **798**, 656–664 (2019).
- Hosokawa, H., Tomita, K. & Takashiri, M. Growth of single-crystalline Bi_2Te_3 hexagonal nanoplates with and without single nanopores during temperature-controlled solvothermal synthesis. *Sci. Rep.* **9**, 10790 (2019).
- Cheng, L. *et al.* T-shaped Bi_2Te_3 -Te heteronanojunctions: epitaxial growth, structural modeling, and thermoelectric properties. *J. Phys. Chem. C* **117**, 12458–12464 (2013).
- Yang, L., Chen, Z.-G., Hong, M., Han, G. & Zou, J. Enhanced thermoelectric performance of nanostructured Bi_2Te_3 through significant phonon scattering. *ACS Appl. Mater. Interfaces* **7**, 23694–23699 (2015).
- Soni, A. *et al.* Enhanced thermoelectric properties of solution grown $\text{Bi}_2\text{Te}_{3-x}\text{Se}_x$ nanoplatelet composites. *Nano Lett.* **12**, 1203–1209 (2012).
- Y. Liu, *et al.*, High thermoelectric performance in crystallographically textured n-type $\text{Bi}_2\text{Te}_{3-x}\text{Se}_x$ produced from asymmetric colloidal nanocrystals. *ACS Nano*, **12**, 7174–7184 (2018).

29. M. Hong, *et al.*, N-Type Bi₂Te_{3-x}Se_x nanoplates with enhanced thermoelectric efficiency driven by wide-frequency phonon scatterings and synergistic carrier scatterings. *ACS Nano*, **10**, 4719–4727 (2016).
30. Wada, K., Tomita, K. & Takashiri, M. Fabrication of bismuth telluride nanoplates via solvothermal synthesis using different alkalis and nanoplate thin films by printing method. *J. Cryst. Growth* **468**, 194–198 (2017).
31. Takahashi, M., Asahara, K., Wada, K. & Takashiri, M. Highly productive solvothermal synthesis of hexagonal Sb₂Te₃ fine-platelets using solution with high precursor concentration and added glucose. *Jpn. J. Appl. Phys.* **58**, 055502 (2019).
32. Wada, K., Morikawa, S. & Takashiri, M. Optical and electronic transport properties of single-crystalline Bi₂Te₃ hexagonal nanoplates determined by infrared spectroscopy and first-principles calculations. *Trans. Mater. Res. Soc. Jpn* **43**, 311–317 (2018).
33. Takashiri, M., Kai, S., Wada, K., Takasugi, S. & Tomita, K. Role of stirring assist during solvothermal synthesis for preparing single-crystal bismuth telluride hexagonal nanoplates. *Mater. Chem. Phys.* **173**, 213–218 (2016).
34. Mori, R. *et al.* Improved thermoelectric properties of solvothermally synthesized Bi₂Te₃ nanoplate films with homogeneous interconnections using Bi₂Te₃ electrodeposited layers. *J. Alloys Compd.* **818**, 152901 (2020).
35. Wada, K., Tomita, K. & Takashiri, M. Thermoelectric properties of bismuth telluride nanoplate thin films determined using combined infrared spectroscopy and first-principles calculation. *Jpn. J. Appl. Phys.* **57**, 06HC02 (2018).
36. Hosokawa, Y. & Takashiri, M. Impact of the amount of single-wall carbon nanotubes (SWCNTs) in single-crystalline Bi₂Te₃ nanoplates/SWCNTs nanocomposite films by drop-casting method. *Jpn. J. Appl. Phys.* **58**, SDDG04 (2019).
37. Hosokawa, Y., Wada, K., Tanaka, M., Tomita, K. & Takashiri, M. Thermal annealing effect on structural and thermoelectric properties of hexagonal Bi₂Te₃ nanoplate thin films by drop-casting technique. *Jpn. J. Appl. Phys.* **57**, 02CC02 (2018).
38. Gopal, R. K., Singh, S., Chandra, R. & Mitra, C. Weak-antilocalization and surface dominated transport in topological insulator Bi₂Se₃Te. *AIP Adv.* **5**, 047111 (2015).
39. Neupane, M. *et al.* Topological surface states and Dirac point tuning in ternary topological insulators. *Phys. Rev. B: Condens. Matter* **85**, 235406 (2012).
40. Wang, L.-L. & Johnson, D. D. Ternary tetradymite compounds as topological insulators. *Phys. Rev. B: Condens. Matter* **83**, 241309 (2011).
41. Wiese, J. R. & Muldrew, L. Lattice constants of Bi₂Te₃-Bi₂Se₃ solid solution alloys. *J. Phys. Chem. Solids* **15**, 13–16 (1960).
42. Zhuang, A. *et al.* Screw-dislocation-driven bidirectional spiral growth of Bi₂Se₃ nanoplates. *Angew. Chem. Int. Ed.* **53**, 6425–6429 (2014).
43. Hao, G. *et al.* Spiral growth of topological insulator Sb₂Te₃ nanoplates. *J. Appl. Phys. Lett.* **102**, 013105 (2013).
44. A. A. Chernov, *Modern Crystallography III*, Springer, Berlin pp.104–158 (1984).
45. Bao, L. *et al.* Weak anti-localization and quantum oscillations of surface states in topological insulator Bi₂Se₃Te. *Sci. Rep.* **2**, 726 (2012).
46. Hashibon, A. & Elsässer, C. First-principles density functional theory study of native point defects in Bi₂Te₃. *Phys. Rev. B* **84**, 144117 (2011).
47. Xue, L. *et al.* First-principles study of native point defects in Bi₂Se₃. *AIP Advances* **3**, 052105 (2013).
48. Liu, R. *et al.* Enhanced thermoelectric performance of Te-doped Bi₂Se_{3-x}Te_x bulks by self-propagating high-temperature synthesis. *Crystals* **7**, 257 (2017).
49. Ren, Z., Taskin, A. A., Sasaki, S., Segawa, K. & Ando, Y. Large bulk resistivity and surface quantum oscillations in the topological insulator Bi₂Te₂Se. *Phys. Rev. B: Condens. Matter* **82**, 241306 (2010).
50. Xiong, J. *et al.* Quantum oscillations in a topological insulator Bi₂Te₂Se with large bulk resistivity (6cm). *Physica E* **44**, 917–920 (2012).

Acknowledgements

This study was partly conducted in a collaborative project with Tokai University and Tokyo Metropolitan Industrial Technology Research Institute and was partly supported by Tokai University General Research Organization Grant. The authors wish to thank Prof. Okimura and Prof. Tomita at Tokai University for valuable discussions, and S. Tsuda, A. Kobayashi, M. Yamaguchi, K. Kodaira, H. Watanabe and S. Imaizumi at Tokai University for providing support for the experiments.

Author contributions

M.T. gestated the idea and designed the experiments. Y.K. and M.T. completed the main manuscript text. The experiments and data analysis were conducted by Y.K., R.M., S.Y., and H.Y. with help from H.N. and Y.O. All the authors discussed the results and commented on the manuscript.

Competing interests

The authors declare no competing interests.

Additional information

Supplementary information is available for this paper at <https://doi.org/10.1038/s41598-020-63374-0>.

Correspondence and requests for materials should be addressed to M.T.

Reprints and permissions information is available at www.nature.com/reprints.

Publisher's note Springer Nature remains neutral with regard to jurisdictional claims in published maps and institutional affiliations.



Open Access This article is licensed under a Creative Commons Attribution 4.0 International License, which permits use, sharing, adaptation, distribution and reproduction in any medium or format, as long as you give appropriate credit to the original author(s) and the source, provide a link to the Creative Commons license, and indicate if changes were made. The images or other third party material in this article are included in the article's Creative Commons license, unless indicated otherwise in a credit line to the material. If material is not included in the article's Creative Commons license and your intended use is not permitted by statutory regulation or exceeds the permitted use, you will need to obtain permission directly from the copyright holder. To view a copy of this license, visit <http://creativecommons.org/licenses/by/4.0/>.

© The Author(s) 2020